A Conceptual Design for Deflection Device in VTDP System

Yongwei Gao (gyw630@nwpu.edu.cn)
Northwestern Polytechnical University https://orcid.org/0000-0001-7026-9273
Jianming Zhang
Northwestern Polytechnical University
Long Wang
Northwestern Polytechnical University
Bingzhen Chen
Northwestern Polytechnical University
Binbin Wei
Northwestern Polytechnical University

Research

Keywords: vectored thrust ducted propeller, conceptual design, wind tunnel experiment, numerical simulation

Posted Date: October 15th, 2020

DOI: https://doi.org/10.21203/rs.3.rs-64863/v2

Version of Record: A version of this preprint was published at Advances in Aerodynamics on January 21st, 2021. See the published version at https://doi.org/10.1186/s42774-020-00050-x.

Abstract

The effectiveness of the Vectored Thrust Ducted Propeller (VTDP) system is not high currently, especially the lateral force is not large enough. Thus, a conceptual design for a deflection device of a VTDP system was proposed to achieve effective hovering control. The magnitude of the lateral force that was applied to maintain balance while hovering was examined. A comparison between the experimental and numerical results for the 16H-1 was made to verify the numerical simulation approach. The deflection devices of the X-49 and the proposed design were analyzed using numerical simulations. The results indicated that a larger lateral force and lower power consumption were presented in the proposed design. The results of this article provide a new idea for the design of the VTDP system.

1 Introduction

A traditional helicopter with a tail rotor is limited in its forward flight speed due to the compressibility effect of the advancing blades and flow separation of the retreating blades. The level-flight cruise speed for conventional helicopters is approximately 150 kts . To further enhance the cruise speed, vectored thrust ducted propeller (VTDP) technology was proposed[1-4]. The VTDP system is installed on the aft end of the fuselage and replaces the conventional tail rotor. The VTDP system usually includes a ducted propeller[5, 6], and flow deflection devices. The flow deflection devices can be vertical vanes or other mechanisms. In addition to providing anti-torque and yaw control, the VTDP can provide extra forward thrust and trim control[7, 8]. A compound helicopter with VTDP technology has a higher forward flight speed, better controllability and agility and larger payload capabilities.

The Piasecki 16H and Piasecki X-49 use VTDP systems[9]. The Piasecki 16H was a series of compound helicopters produced in the 1960s. The first version of the Pathfinder, the 16H-1 version, first flew in 1962. A similar but larger Pathfinder II, the 16H-1A, was completed in 1965.The Piasecki X-49 “SpeedHawk” is an American four-bladed, twin-engine, experimental, high-speed compound helicopter under development by Piasecki Aircraft.

Similar deflection devices for the 16H-1 and X-49A are displayed in Fig. 1 and Fig. 2, respectively. The 16H-1 uses vertical vanes as deflection devices, and the X-49A uses a swerving sector (similar to a semi-spherical shell) as a deflection device. During flight, the vanes do not undergo deflection or sector withdrawal. While hovering or yawing, the vanes undergo deflection or sector extension to provide the proper torque.

Hovering for VTDP systems poses more restrictions than forward flight in that hovering state should provide a larger lateral force and a smaller axial force. Different forms of the flow deflection devices are intended to have different effects.

Considering that the effectiveness of the Vectored Thrust Ducted Propeller (VTDP) system is not high currently, especially the lateral force is not large enough, an alternative form of the flow deflection device was proposed in this article. To verify the numerical simulations, the wind tunnel experiments on a ducted

propeller and the VTDP system of the 16H-1 were carried out. After validating the simulation results, simulations were conducted on the VTDP of the X-49 and the proposed conceptual VTDP. The simulated results showed that the proposed flow deflection device was superior to the VTDP systems of the 16H-1 and X-49.

2 Computational Model Validation

Two examples, which were a ducted propeller and the VTDP system of the 16H-1, were used to verify the numerical simulation approach used in this article.

2.1 Experimental equipment and methods

The wind tunnel tests of the two models of the ducted propeller and the VTDP system of the 16H-1were carried out in the NF-3 wind tunnel at Northwestern Polytechnical University, Xi'an, China.

The ducted propeller model was firstly used to verify the numerical simulation approach. An optical sensor was used to measure the rotor speed, and the voltage and current were also measured. The experimental model is shown in Fig. 3 and Fig. 4. The tip clearance ratio is defined as follows:

$$\delta = \frac{\Delta}{R} \tag{1}$$

where Δ is the blade tip clearance, R is the inner radius of the duct, and δ is the tip clearance ratio. The inner diameter of the duct was denoted as D, and tip clearance ratio δ was 0.91%.

Another experimental model which was similar to the VTDP of the 16H-1 was also used to verify the numerical simulation approach. The experiment was performed on the ground. The slide and rear views are displayed in Fig. 5 and Fig. 6, respectively. The detailed model dimensions are listed in Table 1.

The model was set on an experiment table, which contained a six-component balance system connected to the model. An electric motor was connected to the propeller by a transmission shaft. The propeller was driven by the electric motor with a power rating of 100 kW. Because the hovering state was of interest, there was no free stream. While testing, the rotation speeds of the propeller and deflection angles of the vanes were under control. The axial and lateral forces were measured by a balance system. The power of the VTDP was calculated using the electrical current and voltage measurements, and the calibration was carried out before the experiment. The purpose of the experiments was to provide data to compare with the numerical simulations to verify their reliability. After the simulations were complete, a comparison with the experiments was performed.

Table 1 Main parameters

Component	Parameter	Value
Duct	Inlet diameter	644 mm
	Outlet diameter	618 mm
	Length	232 mm
Propeller	Number of blades	6
	Diameter	593 mm
	Hub diameter	75 mm
	Airfoil	ARAD
	Installed angle of blade tip	10°
Horizontal vane	Chord	92 mm
	Span	602 mm
	Airfoil	NACA 0012
Vertical vane	Chord	185 mm
	Span	493 mm / 600 mm / 493 mm
	Airfoil	NACA 0012

2.2 Calculation method and mesh generation

The numerical simulation was performed using ANSYS CFX commercial software. The steady Reynolds-averaged Navier–Stokes (RANS) equations were used to carry out the numerical study. The two-equation SST model was used to simulate the full turbulence flow around the model, and the dimensionless wall spacing $y^+ < 1$ for all the walls. In the interface of rotation domain and static domain, the general connection interface model of Frozen-Rotor was used.

Fig. 7 shows the computational model of ducted propeller. An unstructured grid was used for the calculations. Multiple coordinate systems were established to simulate the relative motion between the propeller and duct. Accordingly, the computational domain was divided into two sub-domains: a rotating domain and a stationary domain[10]. The propeller was in the rotating domain, and the duct was in the stationary domain. The two domains were used to generate computational meshes, as shown in Fig. 8.

Considering the periodicity of the blade rotation and the symmetry of the duct, the stationary surfaces and rotating region were divided into four segments, and only one of them was used in the numerical calculations. The mesh was properly refined along the leading edge of the propeller, the lip of the duct, and the clearance of the tip, as shown in Fig. 8 and Fig. 9. In this example, 15 prismatic grids were arranged on the surface of the propeller, and the grid number in the rotation domain was about 7 million, and that in the static domain was about 8 million.

And the unstructured computational grid of 16h-1 model is shown in Fig. 10. In this example, the grid number of the rotating domain was 13 million, and that of the static domain was about 27 million.

2.3 Comparison of experimental and calculated results

For the ducted propeller, the experimental results were in good agreement with the calculated results as shown in Fig. 11 and Fig. 12.

For the model of 16H-1, the deflection angle Φ of the vertical vanes was fixed at 20°, and the deflection angle of the horizontal vanes was kept at 0° in both the experiments and numerical simulations. The rotation speed of the propeller was adjusted. The comparisons of the axial force, lateral force, and power of the 16H-1 from the experiments and the numerical simulation are shown below.

Fig. 13 displays the comparison of the axial force for different rotation speeds. The results from the first and second experiments, which are, respectively, labeled as “Experiment 1” and “Experiment 2” in the legend, were similar. The calculated axial force was underestimated by less than 10%. However, the trend was similar to that of the experiment. Fig. 14 shows the comparison of the lateral forces for different rotation speeds. The lateral force was slightly overestimated. Nevertheless, the overall trend was the same.

Fig. 15 shows a comparison of the power for different rotation speeds. The power curves for the two experiments and numerical calculations coincided.

These comparisons demonstrated that the numerical simulation has the potential to be used to estimate the VTDP, at least for the axial force, lateral force, and input power. Based on the comparison, the proposed simulation method can be used to further explore the different VTDP configurations.

3 Investigation Of 16h-1

A new conceptual design for the VTDP system was proposed in this section. Its aerodynamic performance was calculated using the numerical simulation approach verified in previous section. The calculated results were compared with those of 16H-1 and X49.

3.1 Results of 16H-1 and X49

In the simulations of 16H-1 discussed in the previous section, the deflection angle of the vertical vanes was fixed. In the simulations discussed in this section, the rotation speed was fixed at n = 6500 rpm, and the deflection angles were varied.

Fig. 16 displays the axial force or thrust at different deflection angles. The black solid line represents the total axial force for the VTDP of the 16H-1, and the red, blue, and dark cyan colors represent the axial force components from the propeller, duct, and vertical vanes, respectively. With the increase in the deflection angle, the thrust of the propeller (red color) increased, the absolute value of the drag of vertical vanes (dark cyan color) increased and its direction was opposite to that of force produced by the propeller. Meanwhile, the thrust of duct (blue color) reduced. As a result, the whole thrust of the VTDP system decreased monotonically.

Fig. 17 shows the lateral force at different deflection angles. The total lateral forces of the system and the vanes increased first and then decreased. The maximum forces occurred near Φ = 40°. The lateral force of the duct decreased with the increase in Φ.

Fig. 18 shows the power variations at different deflection angles. The maximum consumed power occurred at the same deflection angle as that of the maximum lateral force in Fig. 17.

The numerical simulation results for the X-49 were similar to those for the 16H-1. As shown in Fig. 19, the outer deflector completely opened, and the deflection angles of the vertical vane were 50° and 60°. The numerical results are shown in Table 2.

Table 2 Numerical results for X-49

Deflection angle of vanes	Axial force/N	Lateral force/N	Power/kW
50°	263	306	19.54
60°	208	304	19.40

3.2 Conceptual Design for the Deflection System of VTDP

The conceptual design for deflection system is displayed in Fig. 20. In the conceptual design, the duct was prolonged, eliminating the horizontal and vertical vanes of the 16H-1. Two rotatable slices that were parts of the prolonged duct replaced the extra outer deflector in the X-49. As displayed in Fig. 21, the first slice rotated in an anticlockwise direction, and the second slice rotated in a clockwise direction. While operating, the two slices constituted a nozzle that was similar to a vectored thrust nozzle.

Fig. 22 shows the grid at the horizontal central section. Fig. 23, Fig. 24 and Fig. 25 show the variations of the axial force, lateral force, and power with the deflection angle Ψ of the rotating slice. In these figures, “VTDP system” represents conceptual deflection system of VTDP as shown in Fig. 20, the “Propeller” represents the propeller in the VTDP system as shown in Fig. 20(a), the “Duct” represents the duct in the VTDP system as shown in Fig. 20, and the “First rotating slice” and the “Second rotating slice” represent the rotating slices in the VTDP system as shown in Fig. 21.

3.3 Comparison of the Results of the Conceptual Design, 16H-1, and X-49

3.3.1 Force and Power

The lateral forces between the three deflection systems are compared in Fig. 26 where only the maximum lateral forces for the 16H-1 and X-49 occurred at $\Phi = 40°$ and $\Phi = 50°$, and the lateral forces for the proposed design at different deflection angles are presented. The maximum lateral force for the 16H-1 was smaller than those of the other two deflection systems. The lateral forces of the proposed design for deflection angles from 90° to 120° were comparable with the maximum force of the X-49, although the maximum lateral force of the proposed design at $\Psi = 110°$ was a bit larger than that of the X-49.

For hovering, a larger lateral force and smaller axial force are preferable. The axial forces for the proposed design at deflection angles less than $\Psi = 120°$ were smaller than that of the 16H-1 at $\Phi = 40°$ and X-49 at $\Phi = 50°$, where these angles corresponded to the maximum lateral forces. This indicated that in a range of deflection angles for the proposed design, the axial force was always smaller than those of the other two systems.

The consumed power for the proposed design was the smallest. These comparisons demonstrated that the proposed design provided a high lateral force with smaller values of the axial force and consumed power.

Table 3 Comparison of calculation results of three configurations

Configuration	16H-1	X-49	Proposed design				
Deflection angle	40°	50°	90°	100°	110°	120°	135°
lateral force/N	181.49	306.63	291.89	297.46	322.36	309.91	264.37
axial force/N	322.03	262.74	100.25	146.44	191.65	249.96	320.07
Power/kW	19.57	19.53	18.93	18.92	19.04	19.09	18.88

3.3.2 Streamlines and Pressure Contours

The streamlines and pressure contours are displayed in Fig. 26, Fig. 27 and Fig. 28, providing further information for the proposed design. According to the principle of momentum conservation, the forces exerted on the VTDP, including the axial and lateral forces, are determined by the pressure on the VTDP, the airflow deflection, and the mass flux, which can be explained by Fig. 29.

3.3 Further Analysis

The axial velocity and pressure of the free stream were V_0 and P_0. The velocity increased and the pressure decreased as the airflow approached the propeller. The pressure before the propeller was P'. After the flow passed through the propeller, the pressure increased to $P' + \Delta P$, and the axial velocity increased to V_1. The area of the propeller disk was A_1, and the area of the outlet was A_2. At the outlet, the velocity further increased, and the pressure decreased to P_0. The flow from the outlet of the duct was assumed to be deflected completely. The average deflection angle of the flow was Φ, and the velocity was V_2. According to the principle of momentum conservation, the overall axial force of the VTDP system was

$$T = \dot{m}(V_2 \cos\Phi - V_0) = \rho A_1 V_1 (V_2 \cos\Phi - V_0) \quad (2)$$

and the overall lateral force was

$$Z = \dot{m} V_2 \sin\Phi = A_1 V_1 V_2 \sin\Phi \quad (3)$$

Based on Eq. 2 and 3, the lateral force of the VTDP was related closely to the mass flux through the duct and the deflection angle of the flow. To increase the lateral force of the VTDP, the mass flux through the duct and/or the deflection angle of the flow should be increased. However, the two variables are coupled, and increasing the deflection angle of the flow would increase the blockage effect, which would lead to a reduction in the mass flux. To obtain the maximum lateral force of the VTDP system, the designer should balance the two variables.

For the VTDP, it is assumed that the deflection angle of the vanes and the deflection angle of the airflow were consistent. From the continuity equation, we obtain the following:

$$A_1 V_1 = A_2 V_2 \cos\Phi \quad (4)$$

For hovering, the incoming airflow velocity is zero. The thrust of the VTDP is

$$T = \dot{m} V_2 \cos\Phi = \rho A_2 (V_2 \cos\Phi)^2 \quad (5)$$

and the lateral force is

$$Z = \dot{m} V_2 \sin\Phi = 0.5 \rho A_2 V_2^2 \sin 2\Phi \quad (6)$$

As indicated by the streamlines at the horizontal central section in the Fig. 26(a)-Fig. 28(a), the 16H-1 caused less airflow deflection than the X-49 and the proposed design. Thus, the 16H-1 yielded a greater axial force and a smaller lateral force, according to the principle of momentum conservation. The deflection devices installed in the X-49 and the proposed design were more effective than the vertical vanes design in 16H-1.

The pressure contours can provide an explanation for the superiority of the designs of the X-49 and the proposed configuration compared to that of the 16H-1. In the momentum analysis, it was assumed that the exit pressure recovered. However, this assumption was not supported by the pressure contours as shown in Fig. 26(b) -Fig. 28(b). For the 16 H-1, a high pressure was present on the left side, balancing the effect of the vertical vanes, which can be seen in Fig. 26(b). In contrast, high pressures were observed on the right side of the X-49 and the proposed design, providing a higher positive lateral force. It is evident that a positive lateral force was beneficial for hovering in the present case.

Another factor for effective hovering is the mass flow. To calculate the flow through a certain surface, two rectangular sections were used to calculate the axial and lateral flow respectively as shown in Fig. 30. In the calculation process, the reference areas of the three different configurations (16H-1, X-49, and the proposed design) were consistent. Table 4 shows the mass flows of the models. The proposed design had the largest mass flow.

The flow analyses, with the aid of the momentum theorem, revealed that the proposed design caused larger flow deflection, a favorable high pressure, and a larger mass flow, which resulted in a larger total lateral force.

Table 4 Mass flows for different deflection systems of VTDP

Mass flow (kg/s)	16H-1	X-49	Present
Axial	13.45	12.16	11.06
Lateral	9.96	12.88	13.62

4 Conclusion

A deflection device for a VTDP system was designed conceptually in this study. Part of the inspiration for the present design was drawn from careful examination of the flow in the VTDP using the principle of momentum conservation, and another was from a comparison of two existing deflection devices: the 16H-1 and X-49. The proposed design aimed to achieve effective hovering control, and therefore, the lateral force was most important. Moreover, the power for the VTDP was taken into consideration. To verify the effectiveness of the proposed design, comparisons between the experiments and numerical simulations were made for the 16H-1. Similar numerical simulations for the X-49 and the proposed design were carried out. The numerical results indicated that the present design provided a larger lateral force with a lower power consumption

Abbreviations

VTDP: vectored thrust ducted propeller

SST: shear-stress transport

Declarations

Acknowledgements

We would like to thank to all the experimental staff of the NF-3 Wind Tunnel for their hand work.

Authors' contributions

All authors have participated equally during the manuscript preparation. The authors have read and approved the final manuscript.

Funding

No funding.

Availability of data and materials

The files supporting the result of this article are available upon request.

Competing interests

The authors have no competing interests.

Nomenclature

R	inner radius of the duct, mm
Δ	tip clearance ratio, -
C_p	pressure coefficient, -
C_x	force coefficient in the *x* direction, -
C_y	force coefficient in the *y* direction, -
n	rotate speed, rpm
Ψ	deflection angle for conceptual design, °
Φ	deflection angle for 16H-1 and X-49, °
Z	ateral force, N
T	axial force, N
W	power, kW

References

1. Huanjin Wang,Zheng Gao,Research on the Scheme of a High-Speed Helicopter [J]. Flight Dynamics, 200, 36(2): 38-42. DOI: 10.3969/j.issn.1002-0853.2005.01.010.
2. Prasetyo Edi, Nukman Yusoff, Aznijar Ahmad Yazid, Catur Setyawan K., Nurkas W, Suyono W. A.. New Design Approach of Compound Helicopter[J]. WSEAS TRANSACTIONS on APPLIED and THEORETICAL MECHANICS. 2008, 3(9): 799-808.
3. Kai Liu,Fuchen Ye. Review and Analysis of Recent Developments for VTOL Vehicles [J]. ADVANCES IN AERONAUTICAL SCIENCE AND ENGINEERING. 2015, 6(2): 127-138,159.DOI: 16615/j.cnki.1674-8190.2015.02.004.
4. Yu Qiu. X-49a "Speed Hawk" Verification Machine [J]. Weapon and Equipment, 2008, 1: 46-47.
5. Jason L. Pereira. HOVER AND WIND-TUNNEL TESTING OF SHROUDED ROTORS FOR IMPROVED MICRO AIR VEHICLE DESIGN, Professor Inderjit Chopra Department of Aerospace Engineering, 2008

6. Jia xu, Ningjun Fan. Research Status and Structural Design of Ducted UAV [J]. AERODUNAMIC MISSILE JOURNAL, 2008,1: 10-12. DOI: 10.16338/j.issn.1009-1319.2008.01.002
7. A.Yetter. Why do airlines want and use thrust reversers? A compilation of airline industry responses to a survey regarding the use of thrust reversers on commercial transport airplanes. NASA Technical Memorandum 109158. 1995.
8. Qi Rao, Mingjian Sheng, Taofeng, Han,Zhidong, Hu,Yali Chen. Research on Engine Thrust Reverser. SCIENCE MOSAIC, 2014. 2, 91-94. DOI: 10.13838/j.cnki.kjgc.2014.02.015.
9. Prasetyo Edi, Nukman Yusoff, Aznijar Ahmad Yazid, Catur Setyawan K., Nurkas W., Suyono W. A.. New Design Approach of Compound Helicopter[J]. WSEAS TRANSACTIONS on APPLIED and THEORETICAL MECHANICS. 2008, 3(9): 799-808.
10. Zhao Zhu, Investigation on Rotor/Stator Interface Processing Method and Ansys is on Configuration and Aerodynamic of Tubine[D]. Master thesis, Nanjing: Nanjing University of Aeronautics and Astronautics, 2008.

Figures

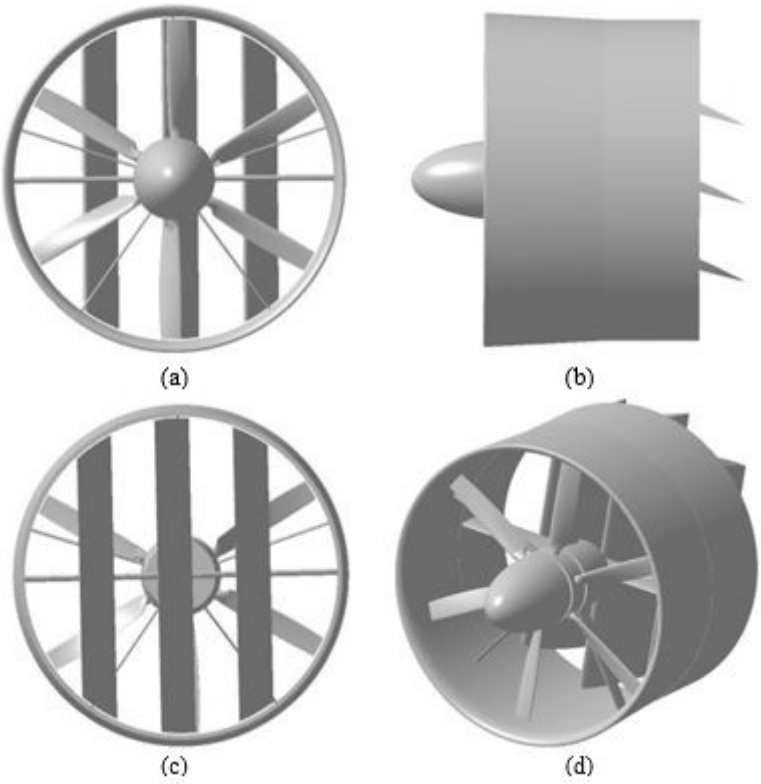

Figure 1

VTDP system for 16H-1

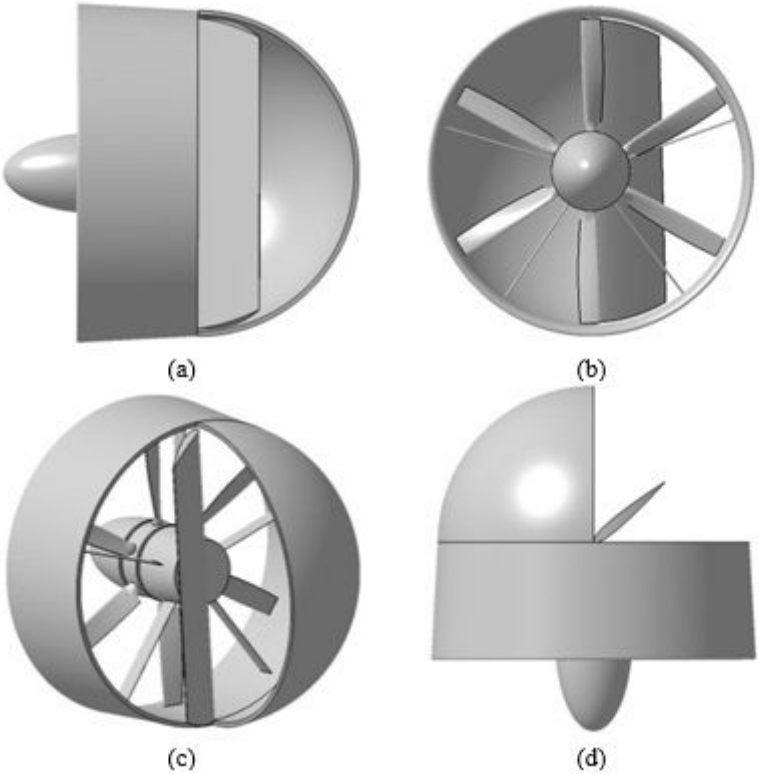

Figure 2

VTDP system for X-49A

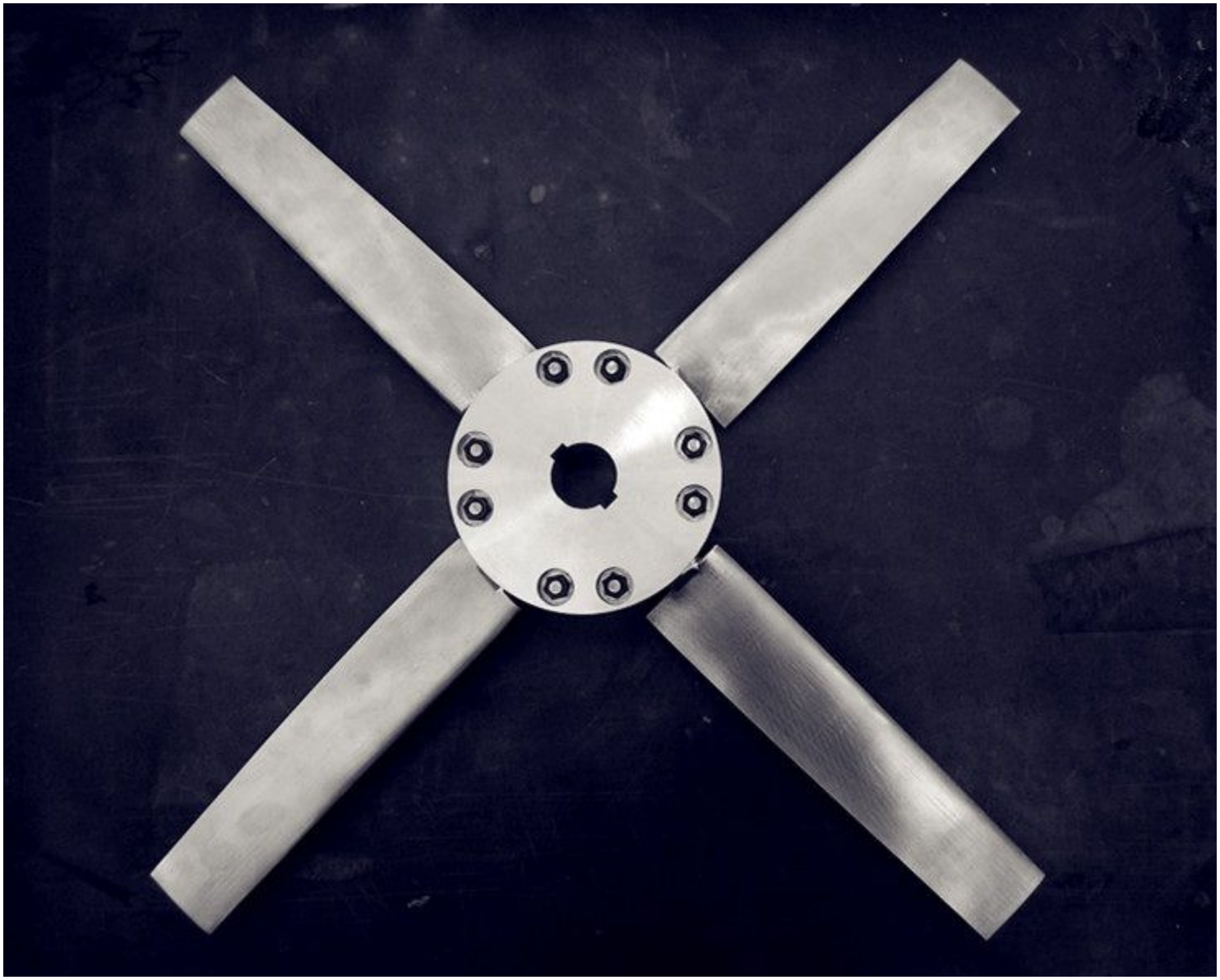

Figure 3

Propeller model

Figure 4

Model of ducted fan experiment

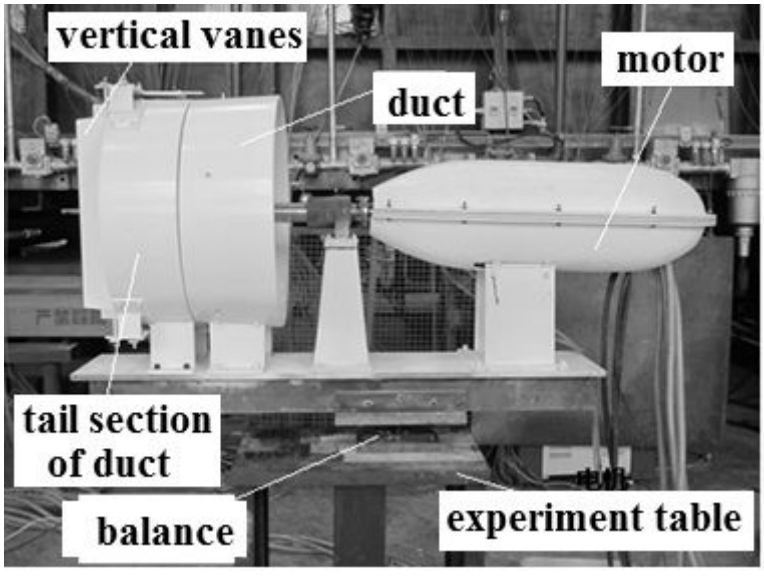

Figure 5

Side view

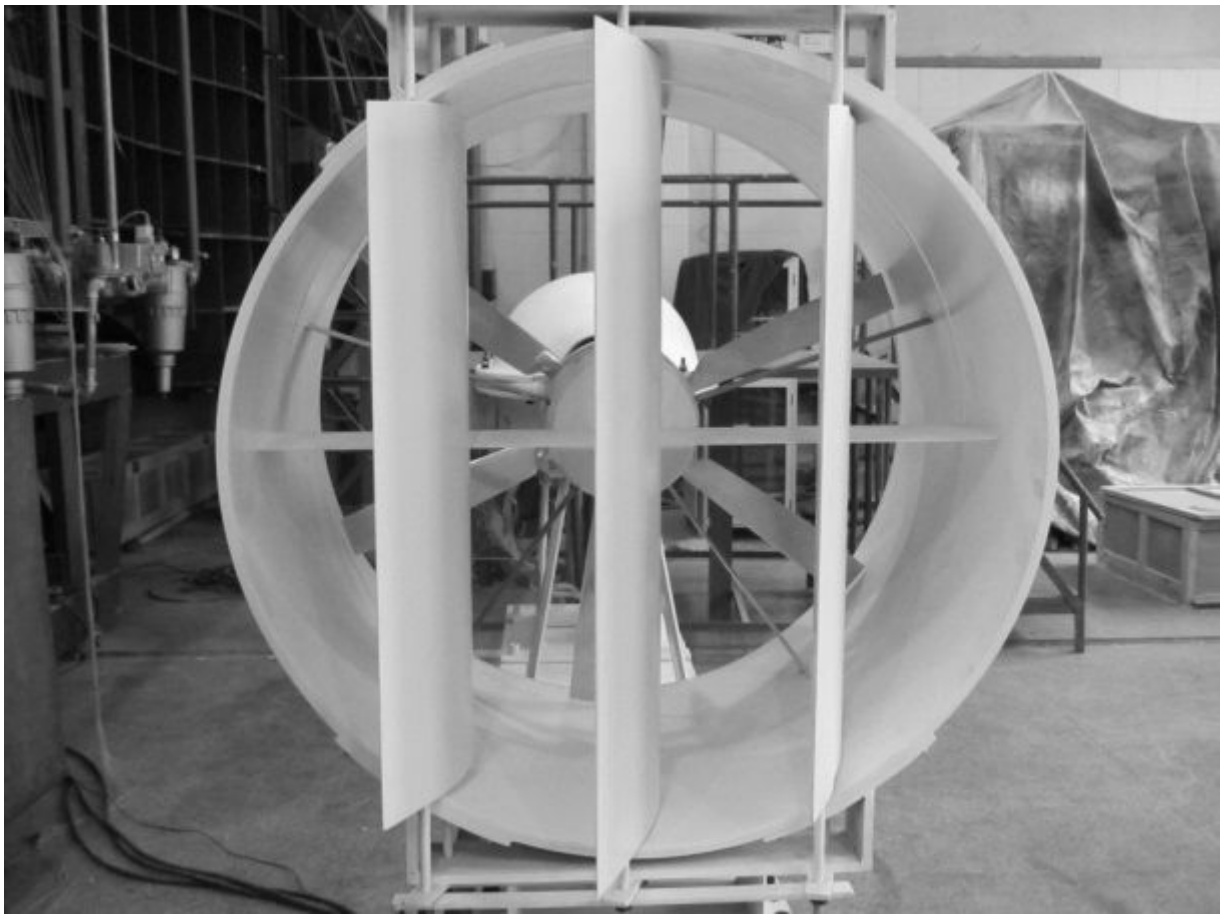

Figure 6

Rear view

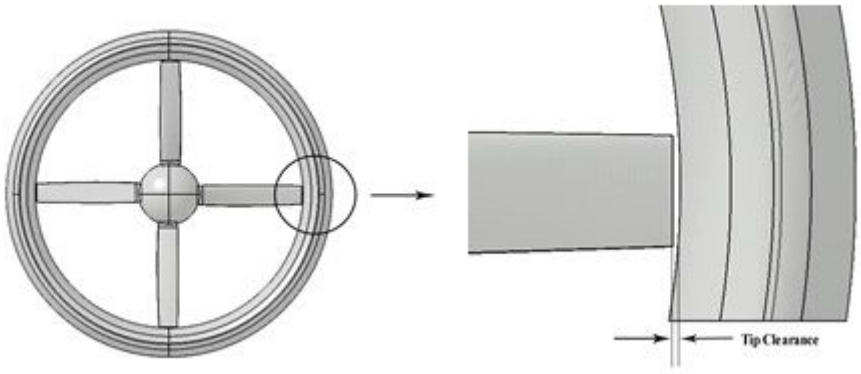

Figure 7

Computational model

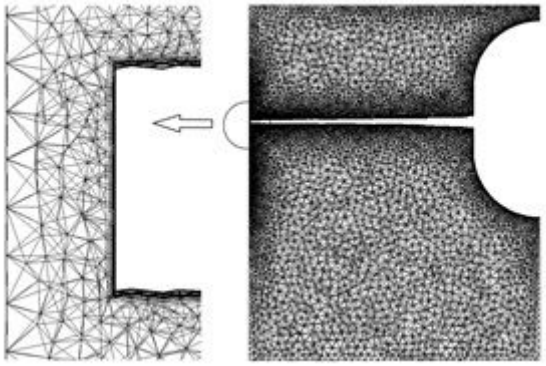

Figure 8

Mesh in the rotating domain

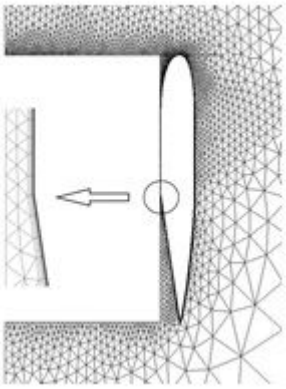

Figure 9

Mesh in the static domain

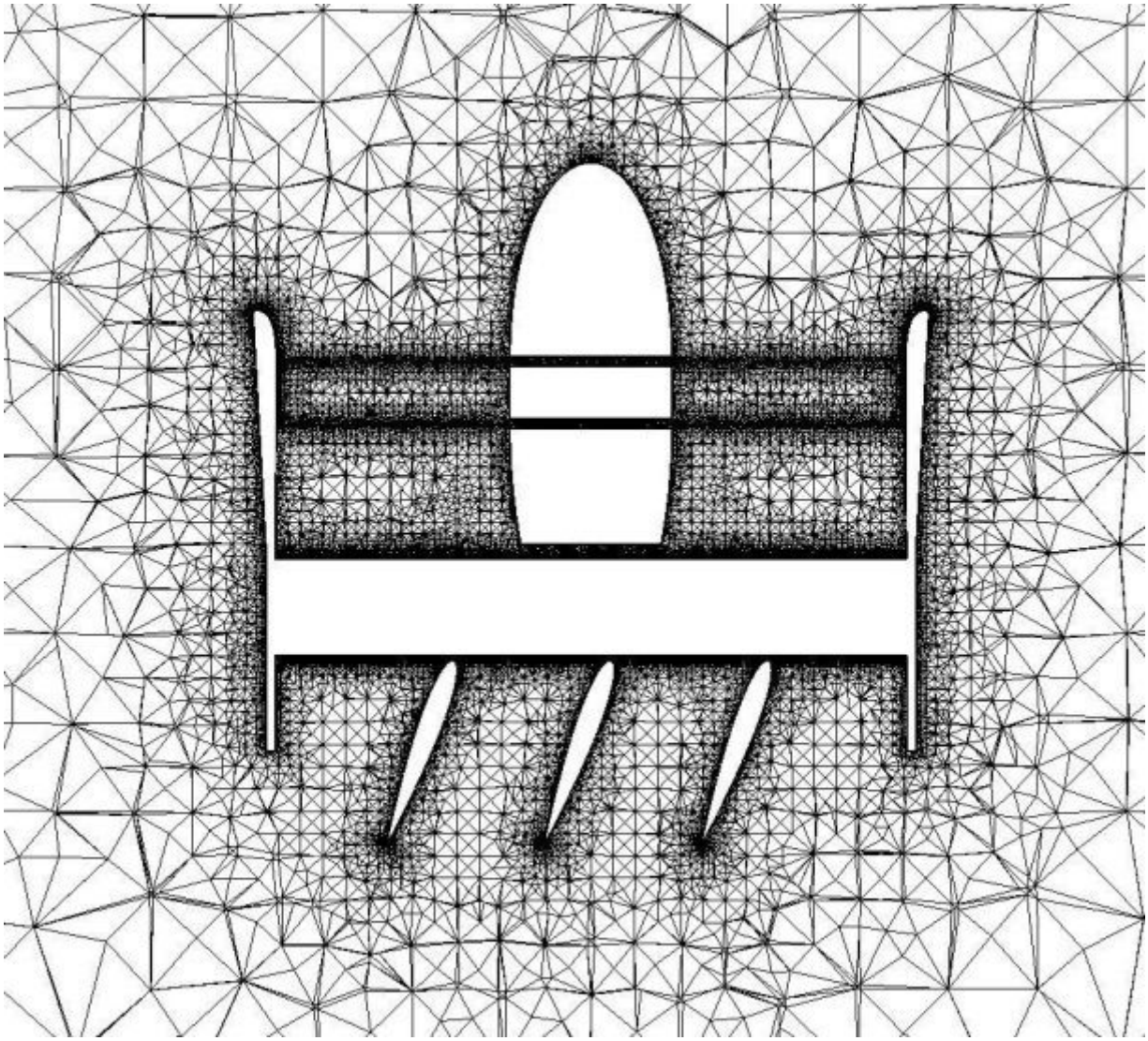

Figure 10

Horizontal central section meshes

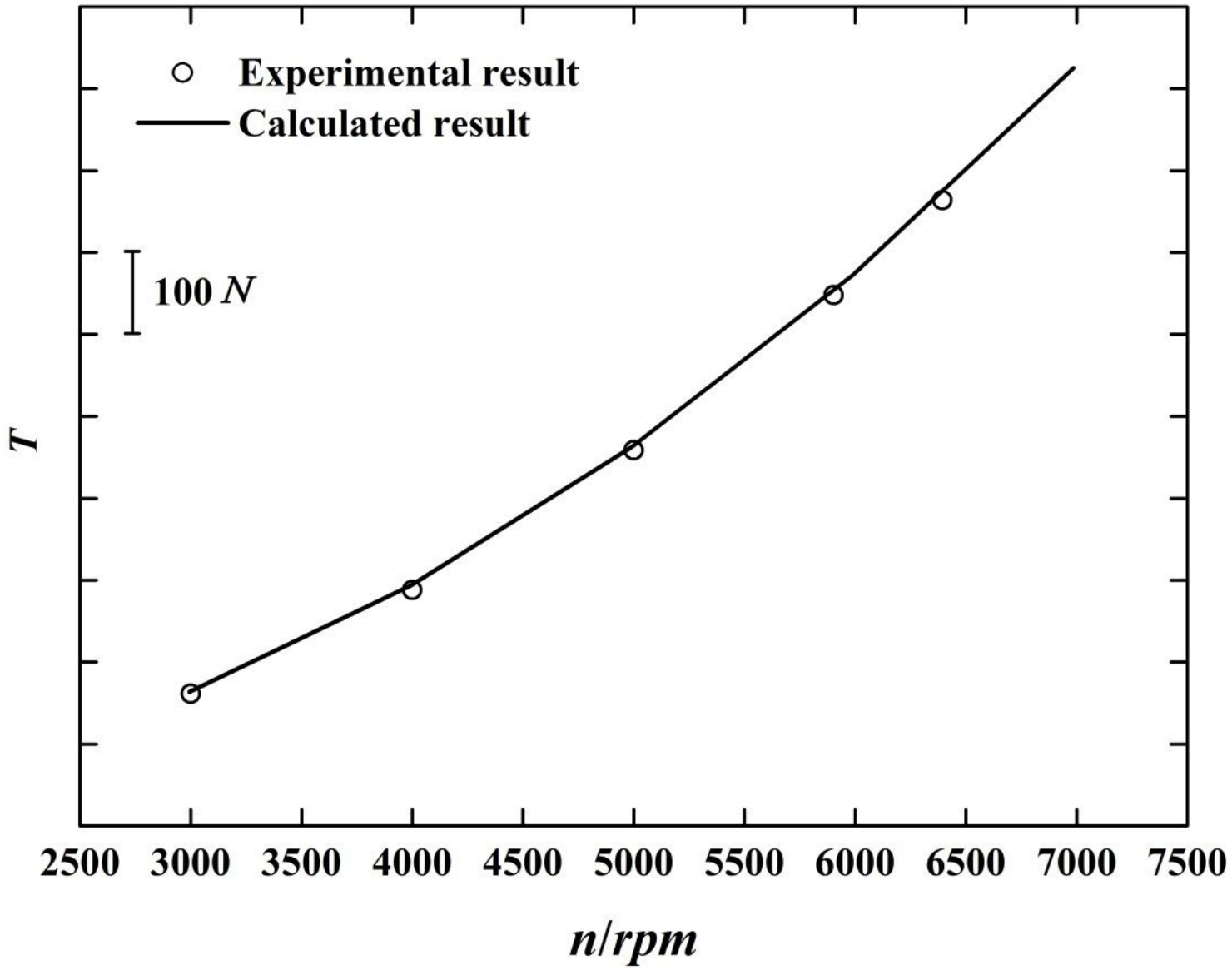

Figure 11

Thrust comparison

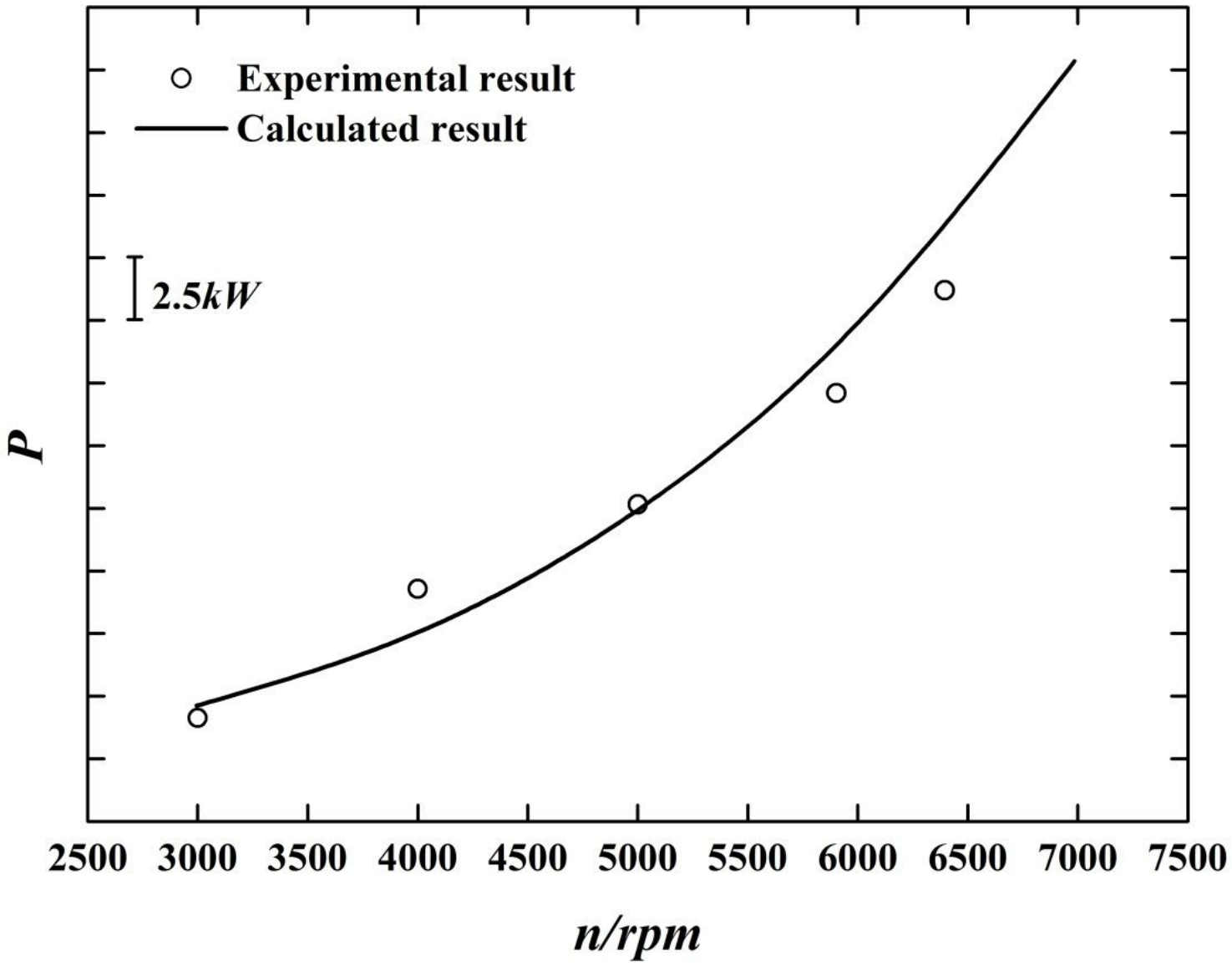

Figure 12

Power comparison

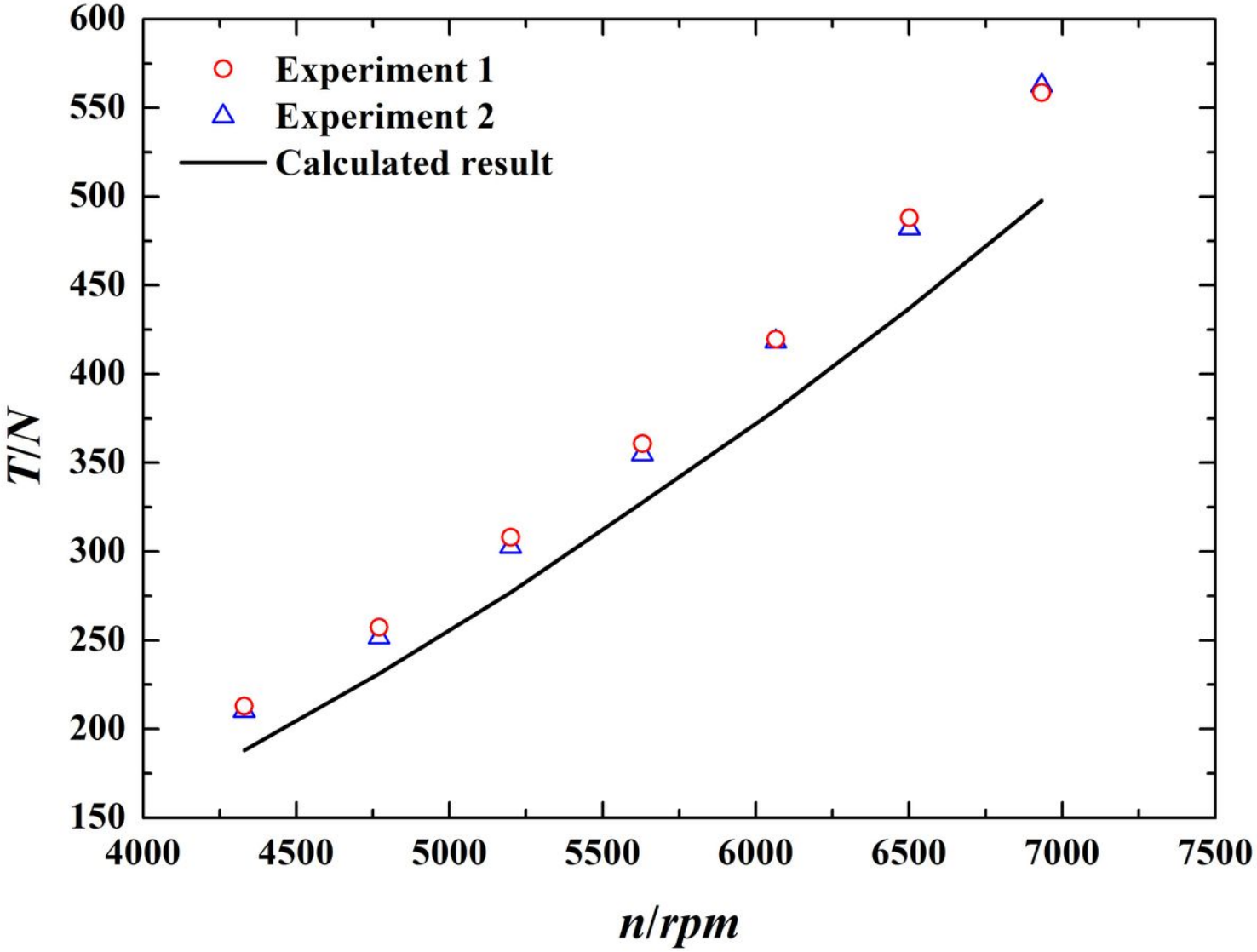

Figure 13

Comparison of axial forces

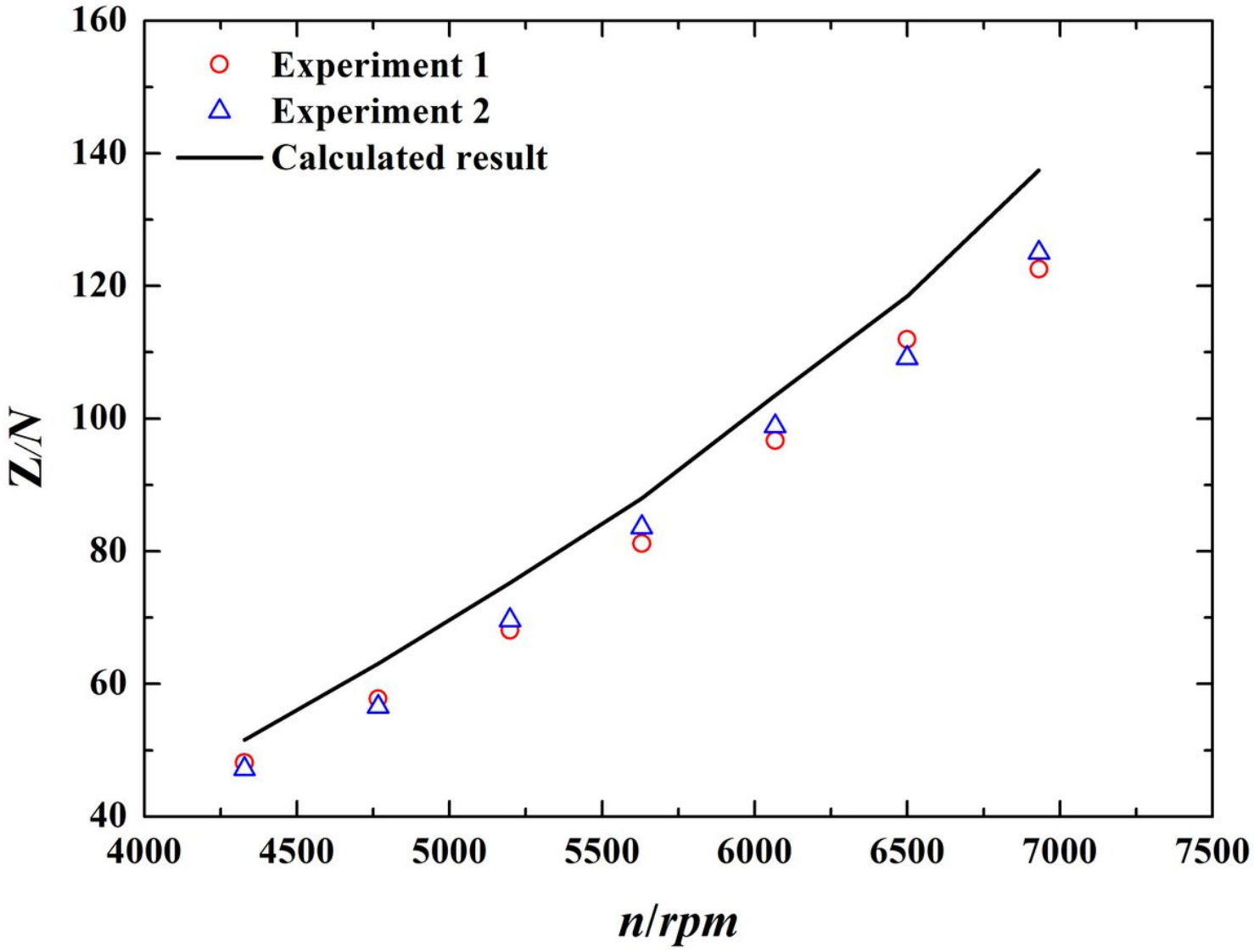

Figure 14

Comparison of lateral force

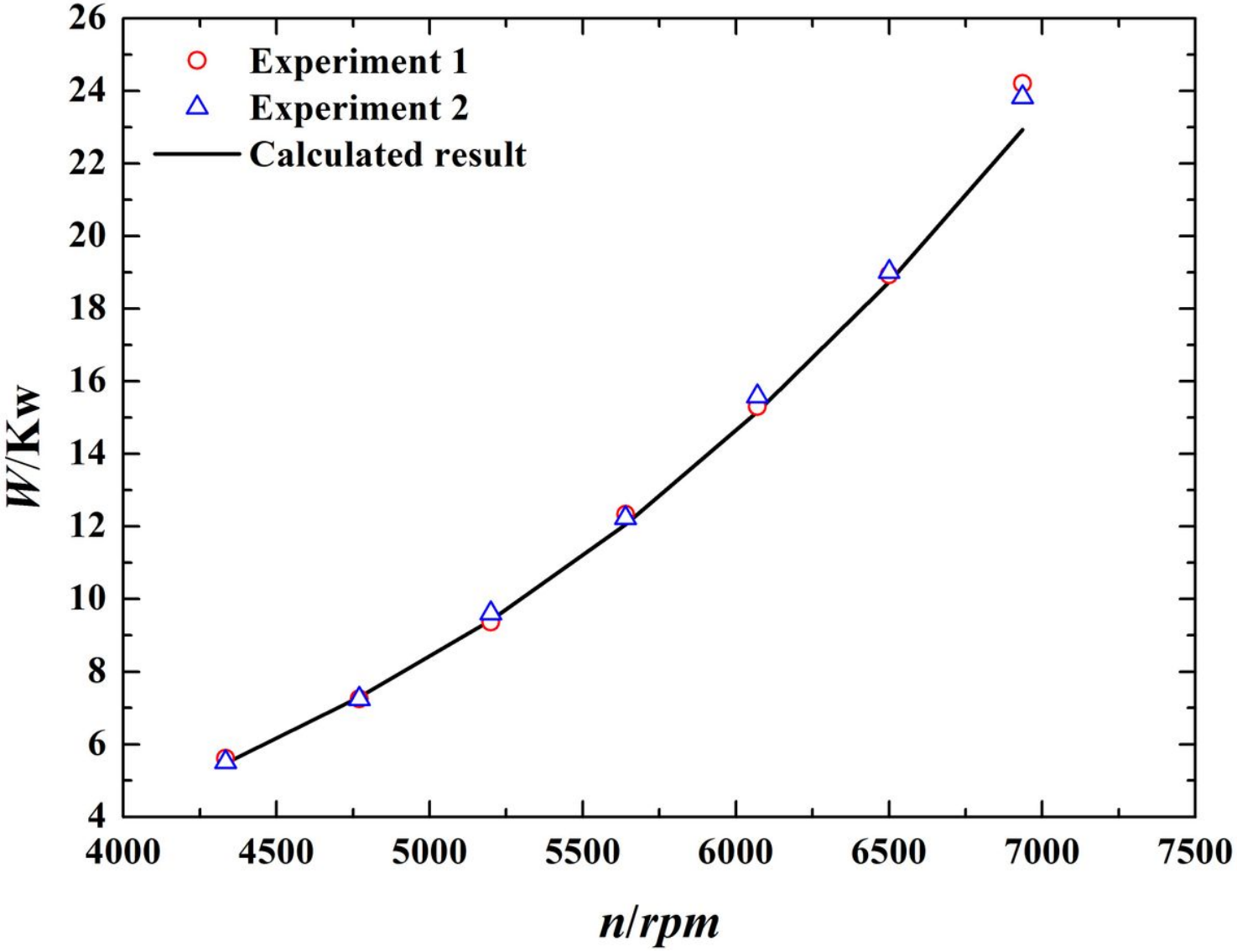

Figure 15

Comparison of power between experiments and calculations

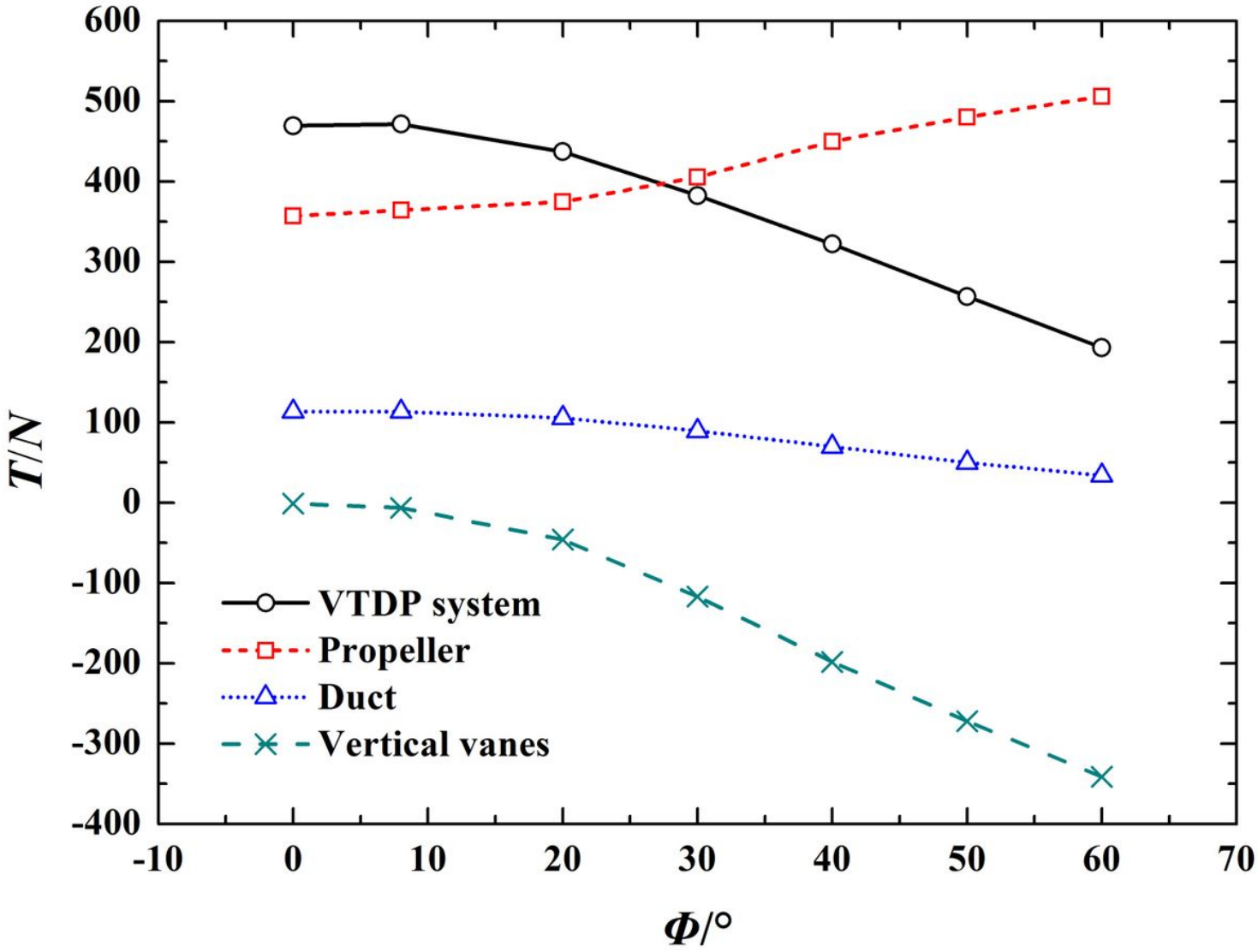

Figure 16

Thrust at different deflection angles

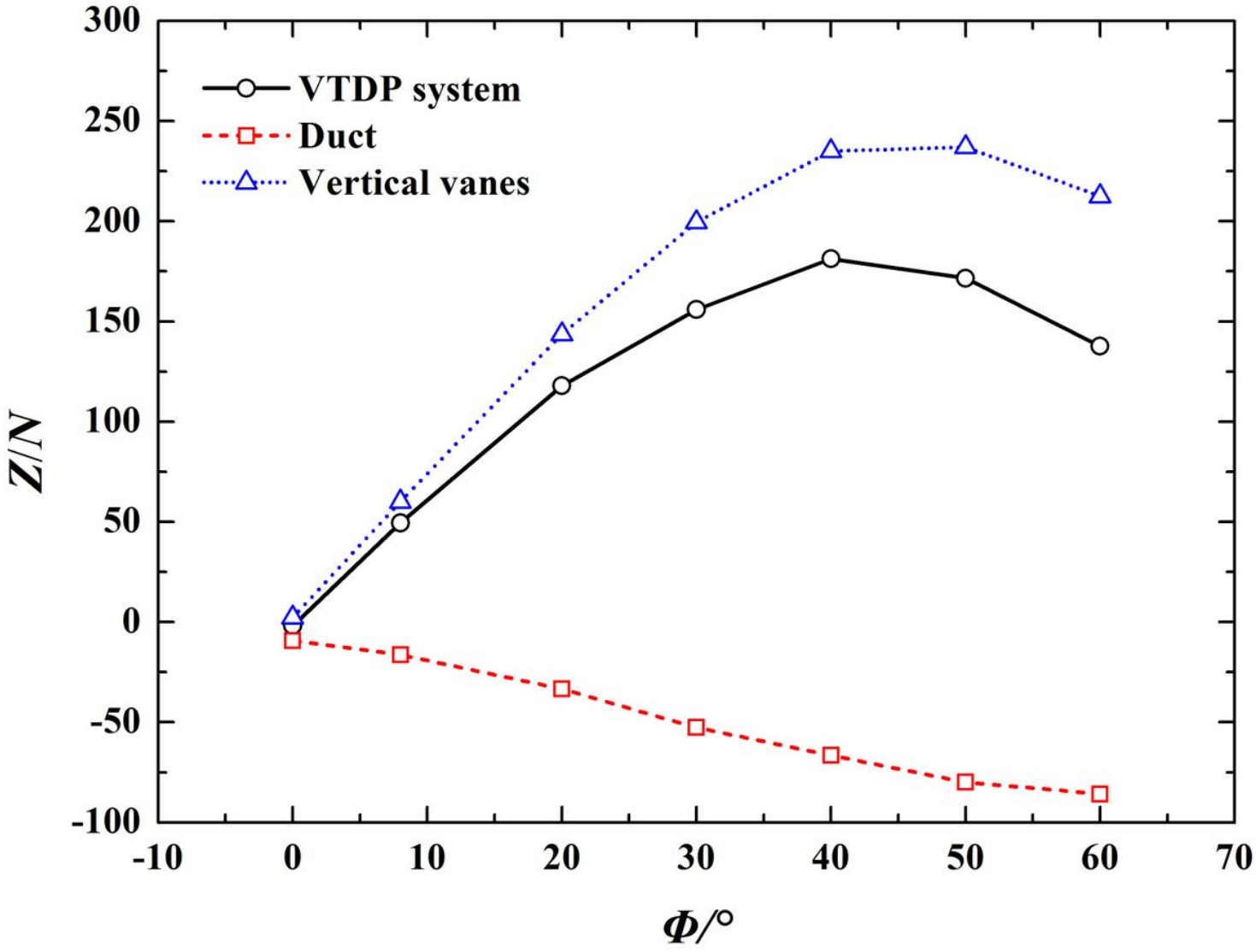

Figure 17

Lateral force at different deflection angles

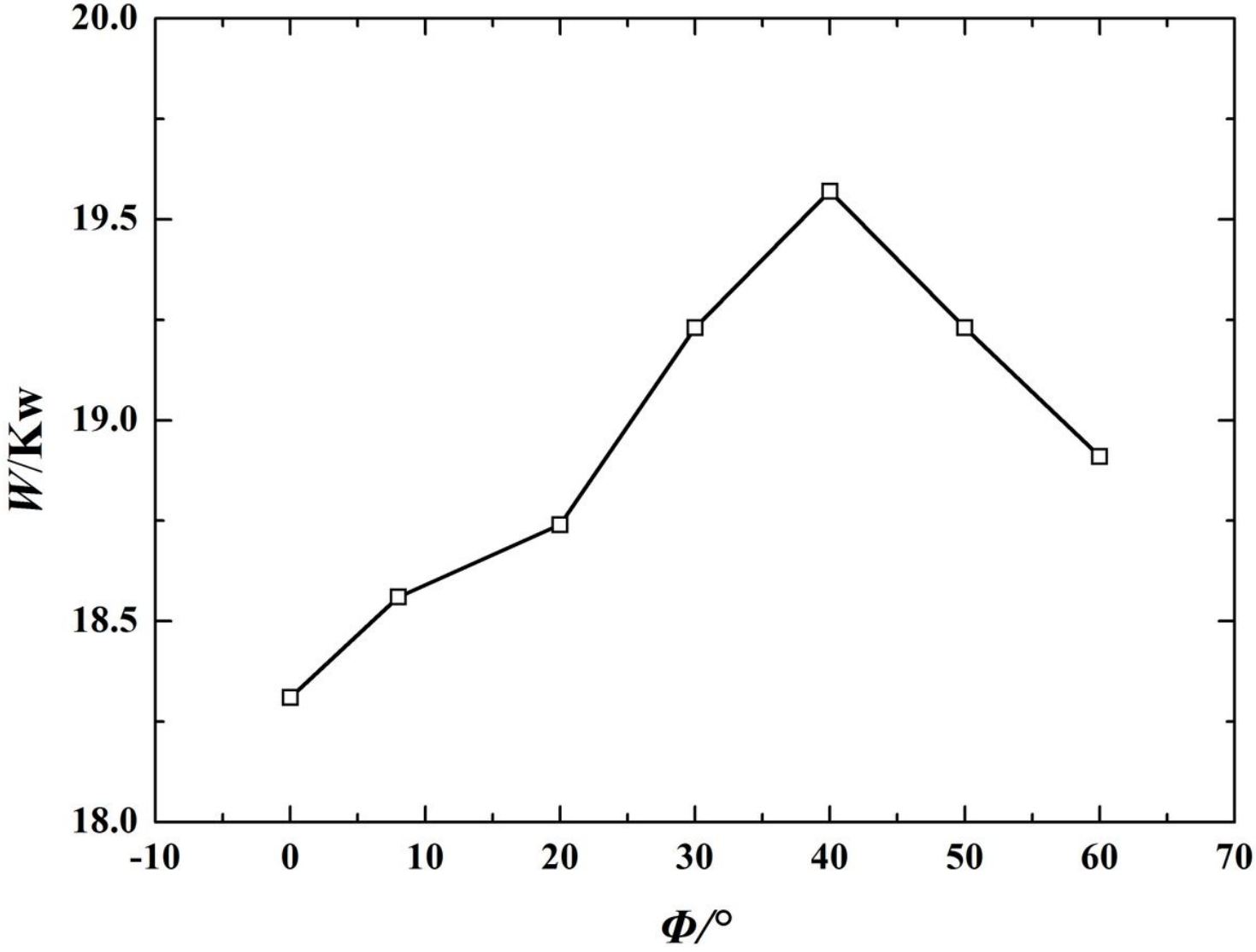

Figure 18

Power at different deflection angles of vanes

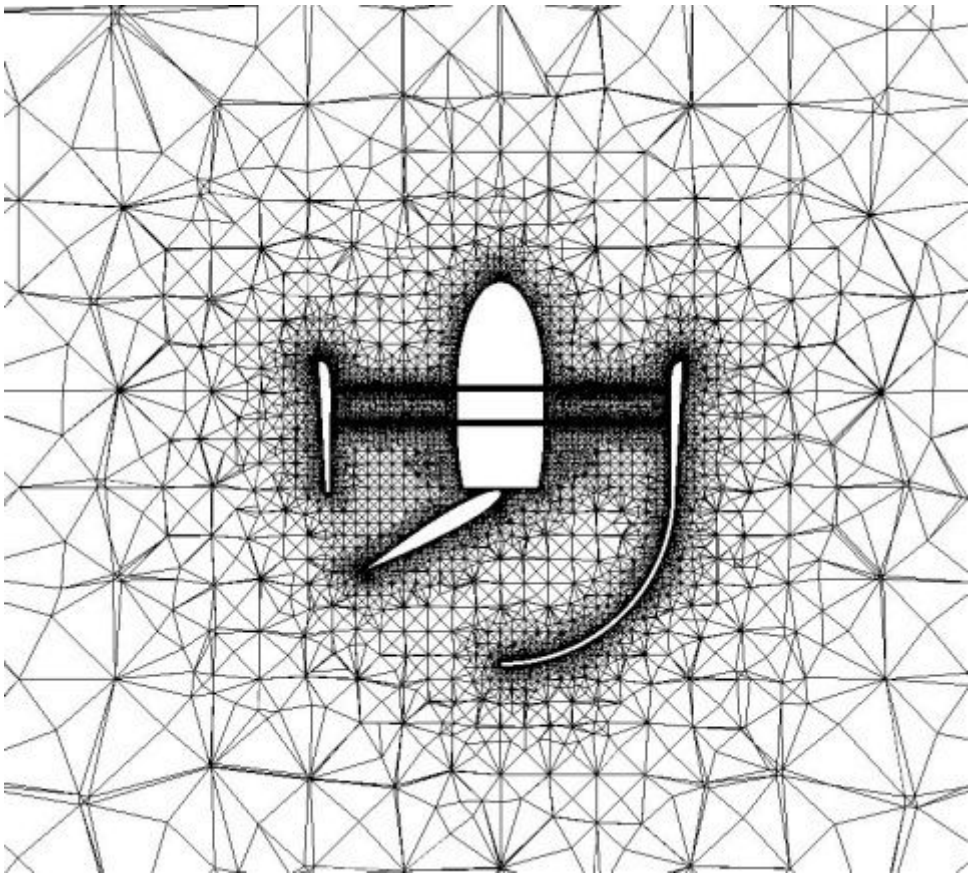

Figure 19

Mesh in the horizontal central section for X-49

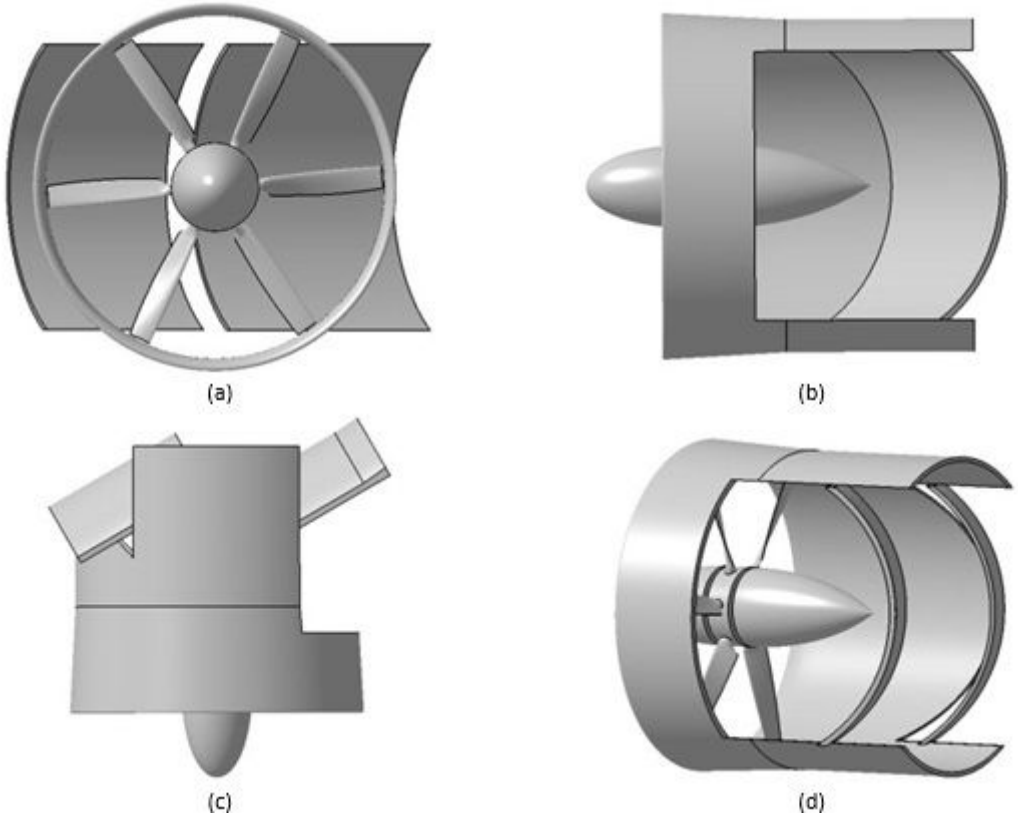

Figure 20

Conceptual deflection system of VTDP. (a) Front view (b) Right side view (c) Top view (d) 3D view

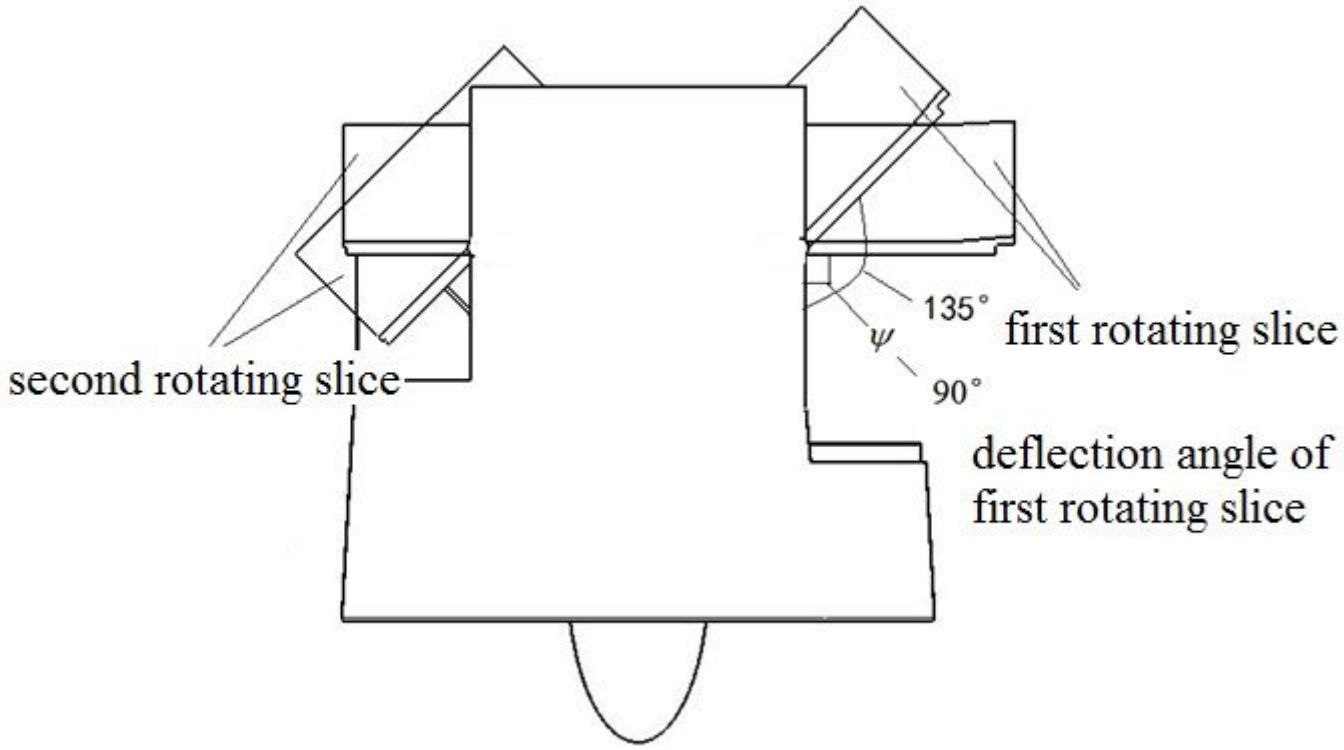

Figure 21

Conceptual deflection system of VTDP at operating conditions

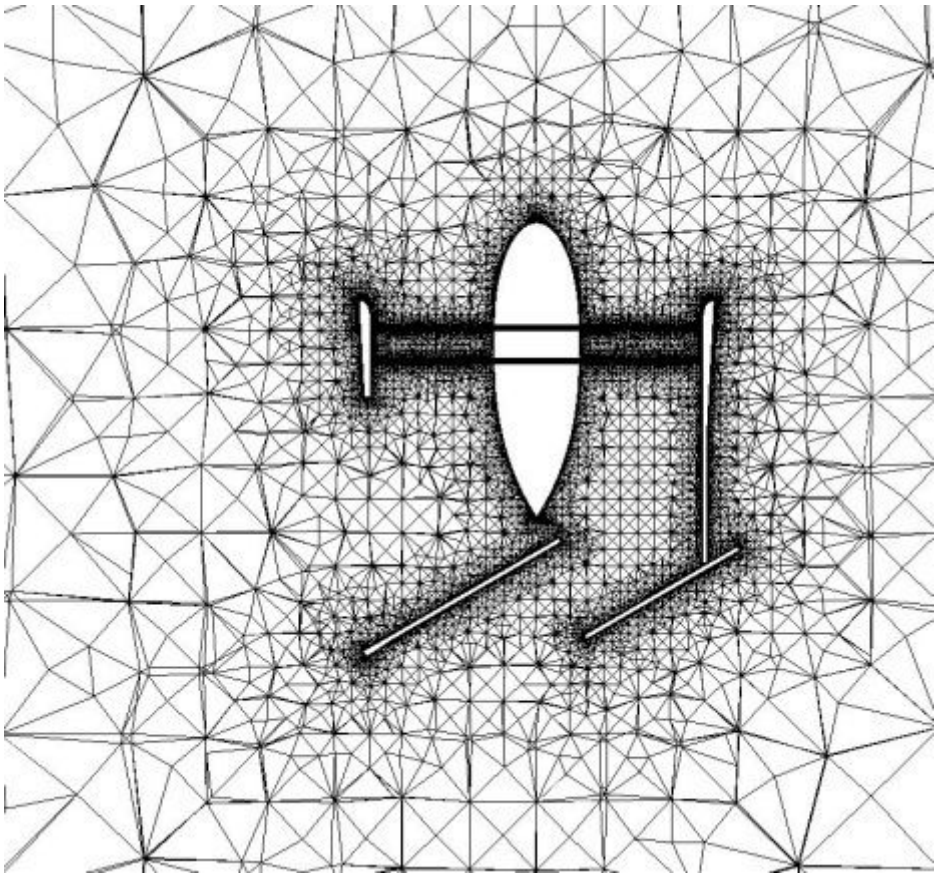

Figure 22

Horizontal central section meshes

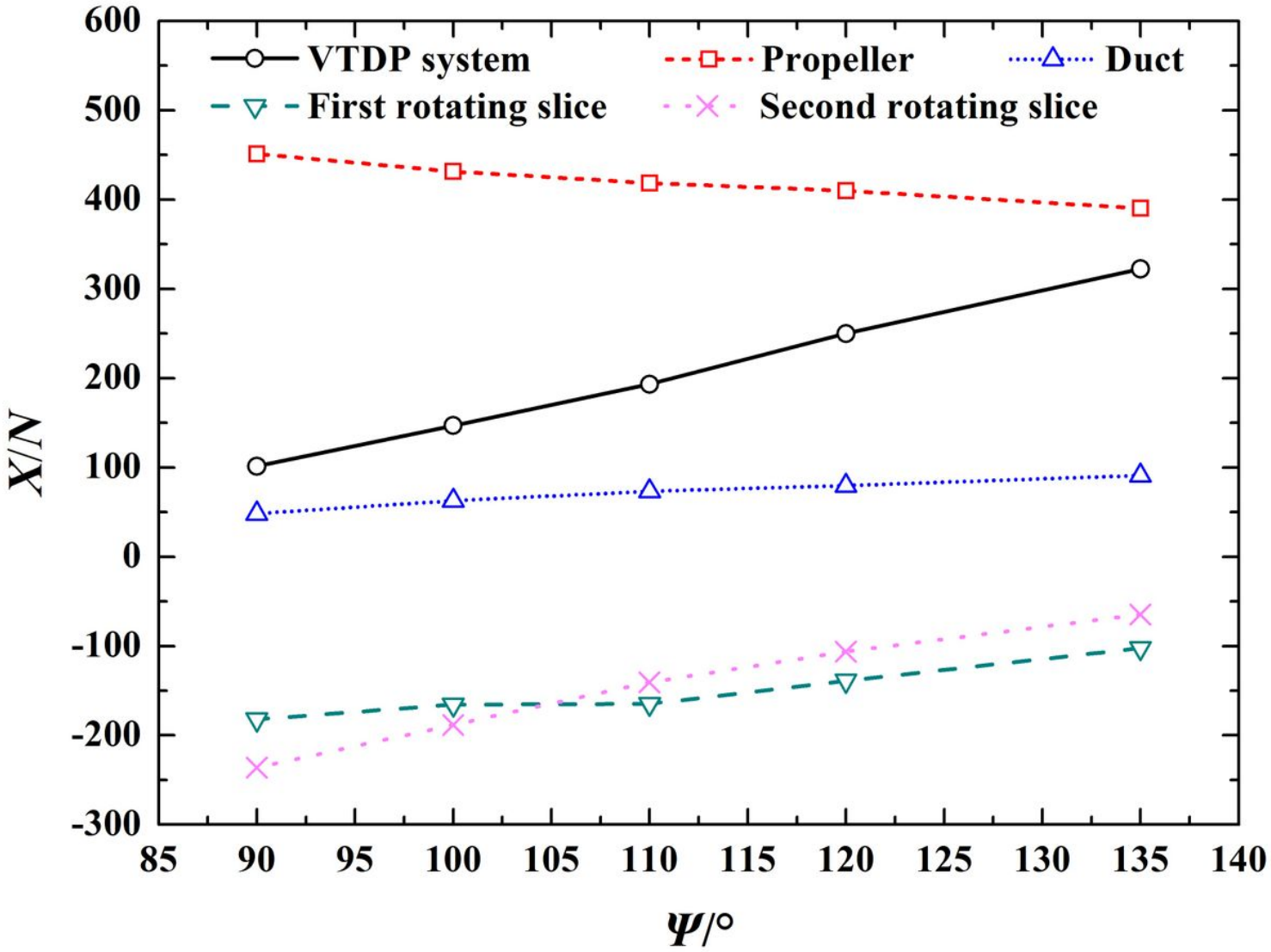

Figure 23

Axial force versus Ψ for conceptual design

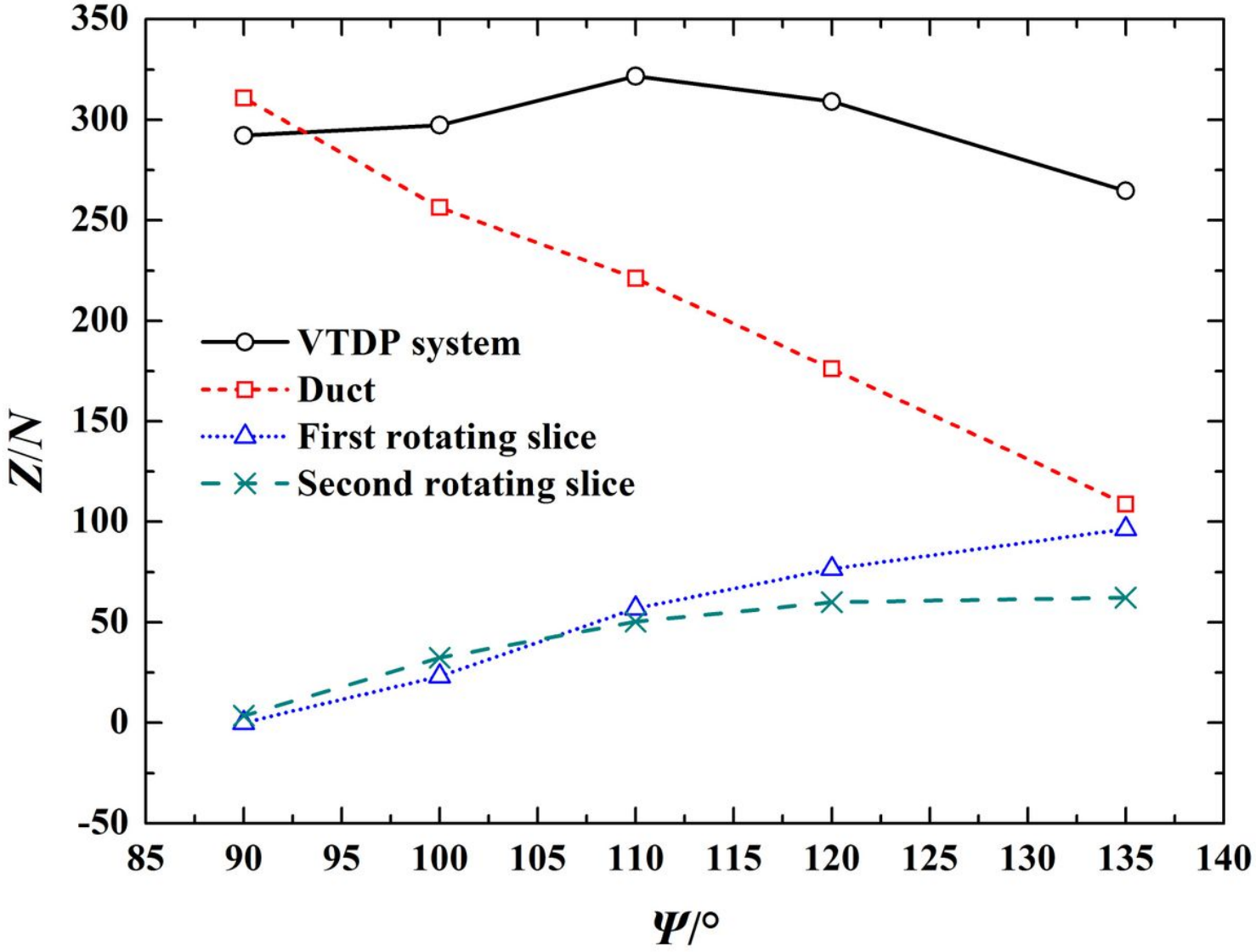

Figure 24

Lateral force versus Ψ for conceptual design

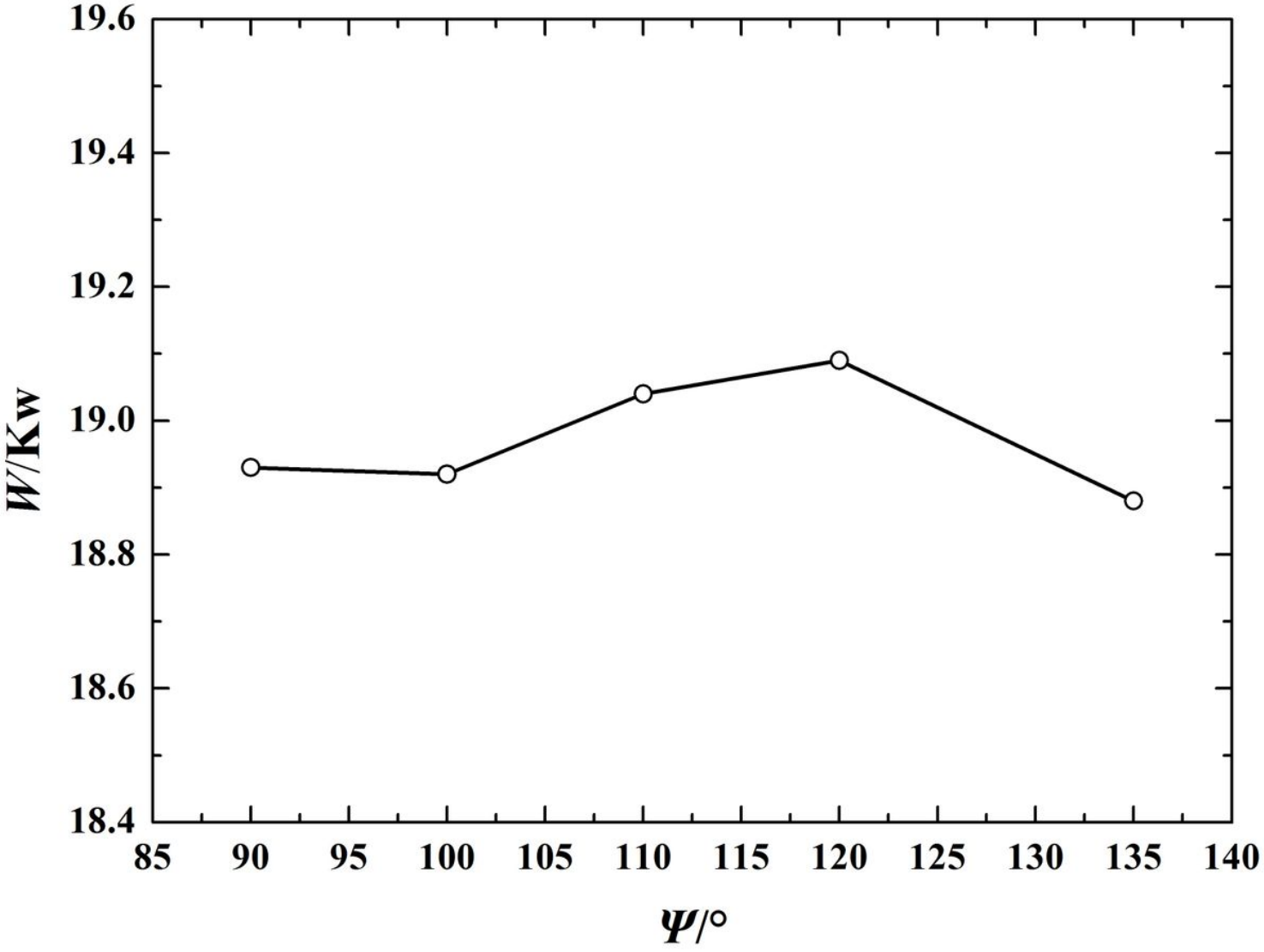

Figure 25

Power versus Ψ for conceptual design

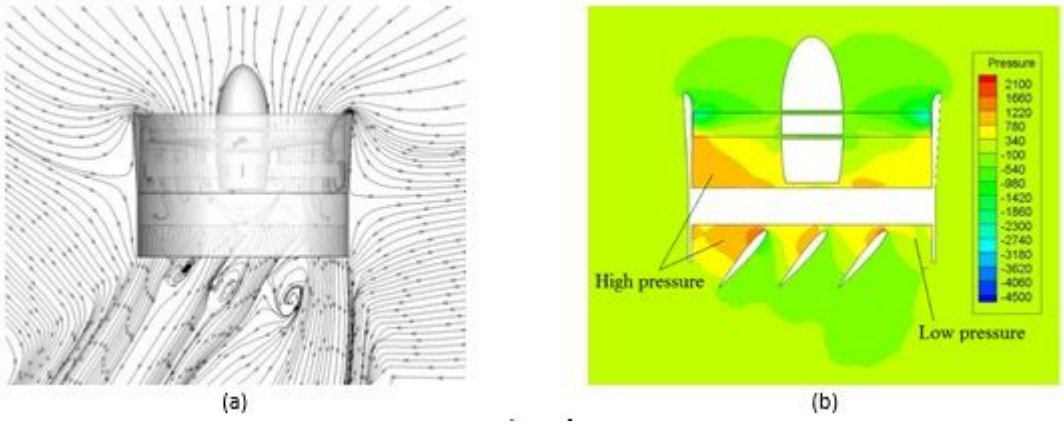

Figure 26

Streamlines and pressure contours for 16H-1 at Φ = 40°. (a) Streamlines (b) Pressure contour

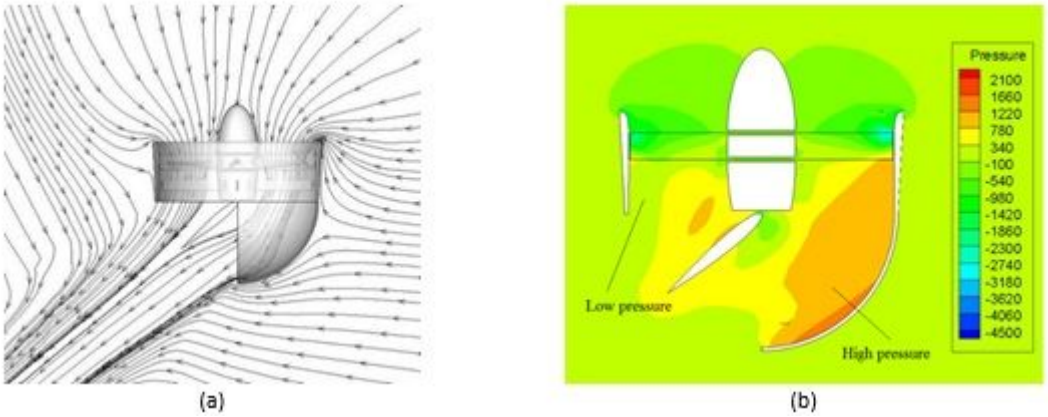

Figure 27

Streamlines and pressure contours for X-49 at Φ = 50°. (a) Streamlines (b) Pressure contour

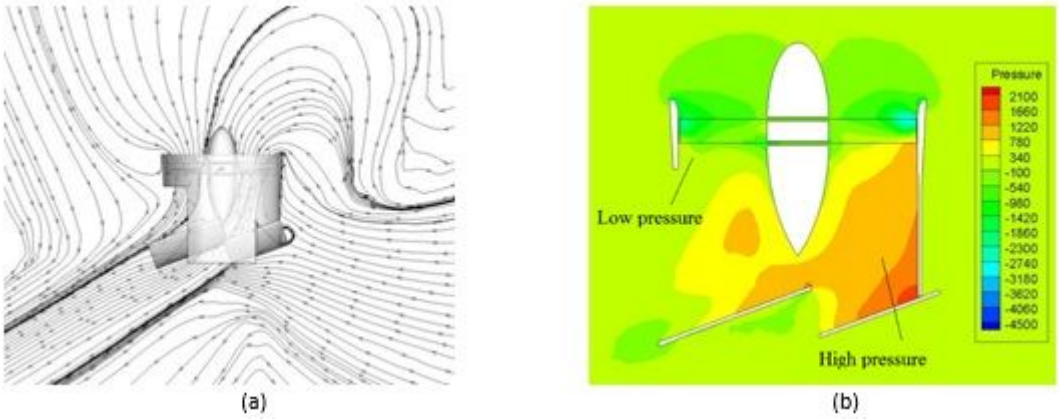

Figure 28

Streamlines and pressure contours for present design at Ψ = 110°. (a) Streamlines (b) Pressure contour

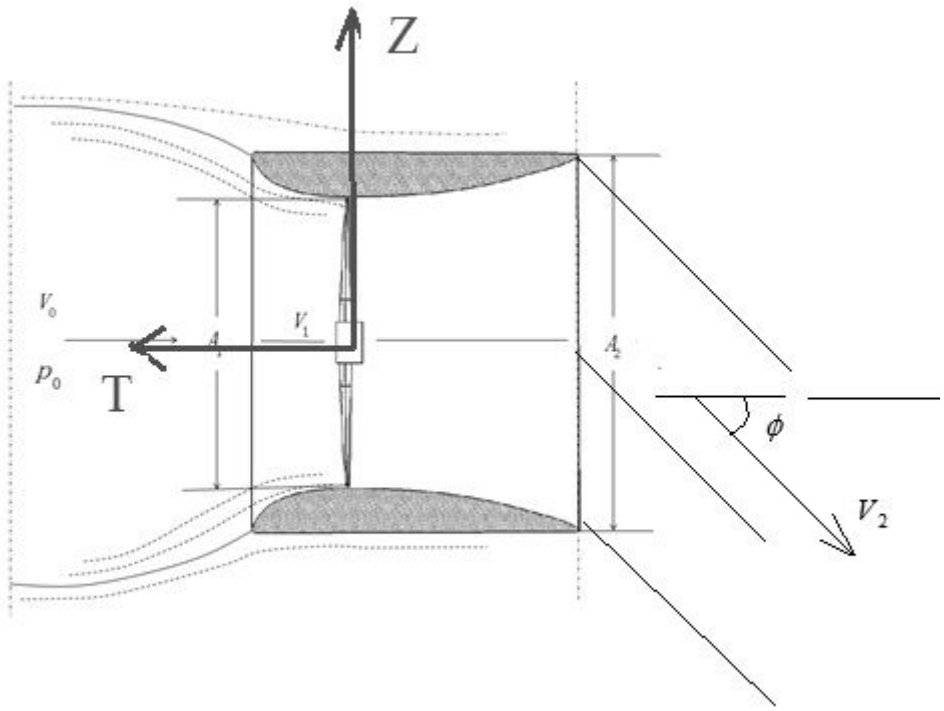

Figure 29

Simplified flow in the VTDP

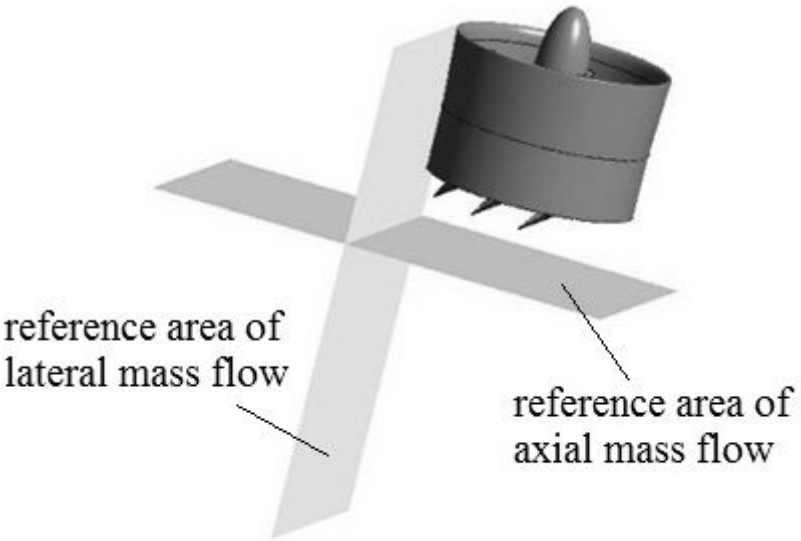

Figure 30

Reference areas for mass flow calculation